



# Interpretation of Phase Formation in Austenitic Stainless Steel Welds

*Criteria for mechanism identification of fully austenitic weld metal formation are recommended*

BY T. IAMBOLIEV, S. KATAYAMA, AND A. MATSUNAWA

**ABSTRACT.** This study aims to reveal the mechanism of fully austenitic microstructure formation and to establish criteria for its identification. Laser spot welds and gas tungsten arc (GTA) welds of alloy Types 310S and 304 were examined. In Type 310S laser beam welds, epitaxial growth of fully austenitic microstructure took place in  $\langle 100 \rangle_{\gamma}$  of the HAZ grain and resulted in just one new weld metal grain. Segregation profiles across the cells were flat. Cracking occurred in the fusion zone. Several ferrite morphologies were found in the Type 304 GTA weld microstructure. Various austenite  $\langle 100 \rangle$ , different from the cell or dendrite growth direction, existed along the dendrites. A shift from duplex to nearly fully austenitic crack-free weld metal was observed in Type 304 laser beam welds irradiated for 1 s to 1 ms. Formation of microstructure by  $\delta$ - $\gamma$  transformation following primary ferritic, but not austenitic, solidification was observed. The identification criteria for the formation mechanism are, first, various austenite  $\langle 100 \rangle$  existing along primary cell growth direction and, second, presence of many new weld-metal grains at the fusion boundary formed seemingly epitaxially from an individual partially melted grain in Type 304 stainless steel.

## Introduction

Five solidification modes have been identified in austenitic stainless steel weld metal under arc welding conditions: austenitic (A), primary austenitic (AF), eutectic (E), primary ferritic (FA), and ferritic (F) (Refs. 1–4). The gradual increase of the ratio  $Cr_{eq}/Ni_{eq}$  results in a shift of the solidification mode from AF to

FA (Refs. 1–3, 5). It may shift within the same fusion zone (Refs. 6, 7). Primary ferritic solidification is required in order to reduce hot cracking, providing a higher solubility of S and P, thus reducing segregation of these impurities (Refs. 8–16). Solid-state  $\delta$ - $\gamma$  transformation results in a duplex microstructure containing a low volume fraction of retained ferrite (Refs. 1–6, 16–20).

It has been recognized that the welding speed rather than the cooling rate affects the solidification mode, favoring the austenite as a first solidifying phase (Ref. 16). The cooling rates encountered in arc welding are on the order of  $10$ – $10^3$  °C/s (Refs. 6, 16). In contrast, cooling rates in the range of  $10^4$ – $6.10^7$  °C/s have been obtained under electron beam and laser beam welding (Refs. 5, 22–26), capacitor discharge welding (Ref. 27) and weld pool quenching (Refs. 7, 22, 28–30) of stainless steel alloys. Under such welding conditions, rapid solidification (RS) takes place in the weld metal (Ref. 31). The formation of high temperature and equilibrium phases can be suppressed by means of a significant undercooling, leading to a variety of new structures including metastable nonequilibrium phases (Refs. 22, 31). It is presumed that an abrupt change in the laser beam weld microstructure of Types 304, 308, 316, and 347 stainless steels must be due to a transition in the solidification mode from primary ferritic to primary austenitic under RS (Ref. 7). However, ev-

idence for this transition is not indisputable. For example, the ferrite appearance in an austenite matrix of a 63 mm/s Type 308 laser beam weld could be due not only to AF solidification mode as stated in Ref. 22 but also to E or even FA mode as well. Instead, based on the dislocation density detected in the weld metal microstructures of alloy Types 308 and 316, it is supposed that possible recrystallization occurs during cooling, subsequent to solidification (Ref. 7). Further, fully austenitic microstructure of a Type 304 laser beam weld has been obtained in Ref. 23 as compared to that of a Type 310S weld; however, there is a lack of evidence for a transition in the solidification mode. A shift in the solidification mode of stainless steel Type 304L as well as of experimental stainless steels has been identified when using electron beam (Refs. 25, 32), laser beam (Ref. 32), and capacitor discharge welding (Ref. 27). A mixed mode of solidification of primary ferrite and austenite has been observed in the fusion zone of Type 308 alloy under capacitor discharge welding. It has been confirmed that the critical cooling rate required for a shift in the solidification mode is composition dependent and increases with increasing  $Cr_{eq}/Ni_{eq}$  ratio of the alloy (Refs. 5, 7, 23, 26, 27). The shift in the solidification mode is attributed to a dendrite tip undercooling (Refs. 7, 22–24, 32, 33). If the barrier to nucleation of austenite can be eliminated then the solidification to metastable austenite can occur at the low solidification rates encountered under GTA welding. Thus, the substrate phase around the melt exerts a great influence on phase selection during RS (Refs. 26, 30, 33, 34). Recent results of laser remelting experiments have confirmed that the ferrite-to-austenite transition shows no nucleation barrier due to subsequent peritectic  $\delta$ - $\gamma$  transformation and is controlled by dendrite-growth kinetics. The austenite-to-ferrite transition occurs at lower Ni

## KEYWORDS

Stainless Steel  
 GTAW  
 LBW  
 Austenite  
 Weldability Testing  
 Alloy 304  
 Alloy 310S

T. IAMBOLIEV is with Department of Manufacturing Technologies, Technical University of Plovdiv, Plovdiv, Bulgaria. S. KATAYAMA and A. MATSUNAWA are with Joining and Welding Research Institute, Osaka University, Osaka, Japan.

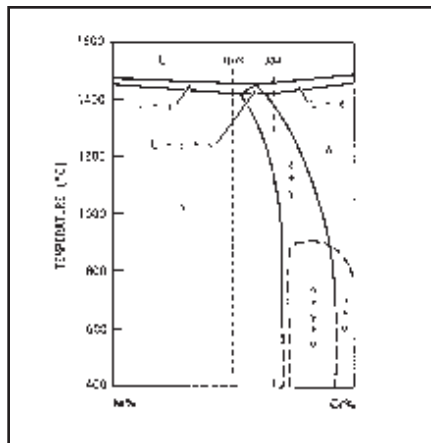


Fig. 1 — Schematic of vertical sections of the Fe-Cr-Ni diagram indicating the location of Types 304 and 310S stainless steel alloys.

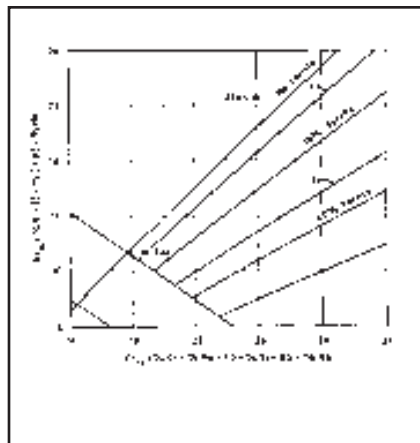


Fig. 2 — Location of Types 304 and 310S stainless steel weld metal in the Schaeffler diagram.

contents than the inverse transition and is controlled by nucleation of ferrite along the growing austenite dendrite front. It is reported that continuity of crystallographic orientation is observed across the  $\delta$ - $\gamma$  and  $\gamma$ - $\delta$  transition fronts and the growth of the peritectic austenite favors the same orientation as ferrite despite the difference in crystal structure. However, confidence index values of the electron backscattered diffraction patterns used, as well as data for orientation relationships supporting this observation, are not provided (Ref. 35). It is indicated that high cooling rates due to RS make microstructure prediction of rapidly cooled weld metal using conventional constitutional diagrams (Refs. 7, 23-26) impossible. Corrections of the phase diagrams have been proposed (Refs. 7, 23, 24). Solidification microstructure selection maps have been calculated in order to predict microstructure morphology and phase formation according to the composition and the growth velocities (Refs. 36, 37).

Previous studies on RS under electron beam and laser beam welding found hot cracks in the fully austenitic weld metal of alloy Types 304L, 316, and 347 solidifying normally as primary ferritic (Refs. 23, 25). On the other hand, no cracking has been detected in the 304, 308, and 316 alloy welds prepared under the same conditions, i.e., the fully austenitic microstructure does not necessarily have to be prone to hot cracking (Refs. 7, 22, 23, 27). Rapid

solidification offers less susceptibility to hot cracking due to the advantage of greatly reduced segregation (Refs. 22, 32). Since cells are reported to be distinguishable in the microstructure (Refs. 5, 16, 27, 30, 32), solidification has not been partitionless. Thus, it is likely that one of the reasons preventing hot cracking in the weld metal could be attributed to a primary ferritic solidification and also that some of the fully austenitic weld microstructures observed are products of a postsolidification  $\delta$ - $\gamma$  transformation. Summarizing the results of earlier studies, it is obvious the solidification behavior of stainless steel welds under RS is still controversial. Therefore, the objective of this investigation was, first, to better understand the mechanism of microstructure formation in Type 304 weld metal under pulsed laser spot welding and, second, to work out a criterion for identification of the formation mechanism.

### Experimental Procedure

The chemical composition and the related  $Cr_{eq}$  and  $Ni_{eq}$  of the two commercial-type stainless steel alloys 310S and 304 used in this investigation are listed in Table 1. Figure 1 presents a schematic representation of vertical sections of the Fe-Cr-Ni diagram showing superimposed compositions of these alloys. Type 310S alloy solidifies as primary austenite under equilibrium conditions, exhibiting a fully

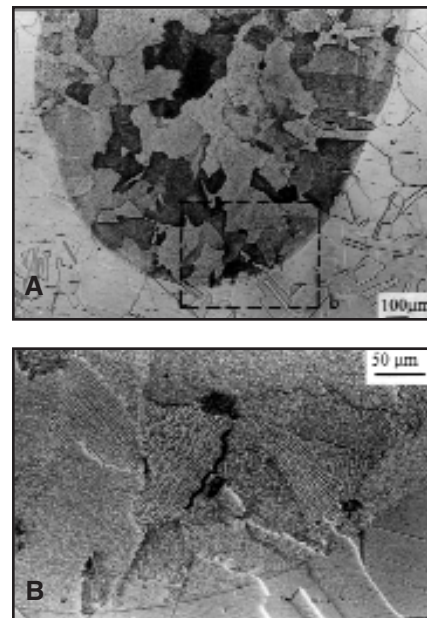


Fig. 3 — Microstructure of a 310S laser spot weld irradiated for 1000 ms at a defocused distance of 10 mm. A — General view in a vertical section; B — bottom of the fusion zone.

austenitic microstructure at room temperature. According to the Schaeffler diagram, the microstructure of the 310S alloy arc welds is also fully austenitic. Type 304 alloy solidifies as primary ferrite and transforms to austenite in solid state on cooling under equilibrium conditions. The transformation  $\delta$ - $\gamma$  is completed below approximately 1100°C and the microstructure becomes fully austenitic at room temperature. The location of Type 304 arc welds in the Schaeffler diagram is shown in Fig. 2 (Ref. 19). Type 304 welds have duplex austenite-plus-ferrite microstructure with about 5% retained ferrite. Plates of Type 310S and 304 alloys with a thickness of 5 mm as well as cast or rolled sheets of the same 304 alloy, 40 mm thick, were homogenized at 1050°C for 100 h prior to welding in order to provoke the occurrence of grain growth. This facilitates the observation of the microstructural relationship between the base and weld metals. Samples sized at 20 × 20 × 5 mm of both alloys cut from the plates were mechanically and chemically cleansed using #400 emery paper and acetone, respectively.

Table 1 — Chemical Composition, wt-%

Material	C	Si	Mn	P	S	Cr	Ni	Cr <sub>eq</sub>	Ni <sub>eq</sub>
310S	0.07	0.61	1.69	0.017	0.002	25.02	19.16	25.94	22.11
304	0.07	0.45	0.82	0.025	0.005	18.16	8.63	18.84	11.14

$$Cr_{eq} = \%Cr + \%Mo + 1.5 (\%Si + 0.5 (\%Nb$$

$$Ni_{eq} = \%Ni + 30 (\%C + 0.5 (\%Mn$$

**Table 2 —Laser Welding Conditions, Cell Spacing, and Cooling Rate of the Weld Metal**

Trial No.	Material	Pulse Energy J	Pulse Duration, ms				Cell Spacing μm	Estimated Cooling Rate, °C/s
			10	15	20	25		
1	310S	1200	1000				2.10 <sup>4</sup> –4.10 <sup>3</sup>	
2		120	100				10 <sup>5</sup> –10 <sup>4</sup>	
3		12	10				2.10 <sup>5</sup>	
4		24		20			1.5.10 <sup>5</sup> –6.10 <sup>4</sup>	
5		12		10			4.10 <sup>5</sup> –2.10 <sup>5</sup>	
6		6				5	—	
7	304	1200	1000			3.5	4.10 <sup>4</sup> –6.10 <sup>3</sup>	
8		120	100			1.4–3	3.10 <sup>5</sup> –4.10 <sup>4</sup>	
9		12	10			0.9–2	5.10 <sup>6</sup> –6.10 <sup>5</sup>	
10		24			20	1.3–2.3	5.10 <sup>5</sup> –6.10 <sup>4</sup>	
11		12			10	1.2–1.3	7.10 <sup>5</sup> –5.10 <sup>5</sup>	
12		6			5	0.9–1.1	1.5.10 <sup>6</sup> –9.10 <sup>5</sup>	
13		1.2			1	—	—	
14		12				10	—	
15		6				5	—	

Shielding gas: Ar with flow rate 15 L/min.

A pulsed NEC Nd-YAG laser delivering 3.2-kW peak power in a pulse wave mode was applied on the sample surface under the conditions displayed in Table 2. The spot welding was performed in Ar shielding gas by 100- or 150-mm focal length lens under defocused distance varying in the range from 10 to 25 mm and laser pulse energy from 1.2 to 1200 J/pulse. Pulse duration varied from 10 ms to 1 s. A Miyachitechnos Co. Nd-YAG laser of 5-kW peak power was also used for welding with a pulse duration from 1 to 20 ms under 20-mm defocused distance in Ar. A 304 sheet sized at 150 × 75 × 40 mm was subjected to autogeneous gas tungsten arc (GTA) welding under the conditions shown in Table 3. The arc length was about 2 mm and a W-Th electrode was used.

The weld spots were transversely sectioned and metallographically polished through 0.1-μm alumina and subsequently etched with either a HNO<sub>3</sub>:H<sub>2</sub>O:HCl=1:2:3 or a 40-g FeCl<sub>3</sub>, 3-g CuCl<sub>2</sub>, 40-mL HCl, and 500-mL H<sub>2</sub>O solution. Microstructural features were studied by means of optical microscopy. SEM and TEM equipped with an EDS detector were used to obtain compositional profiles from pertinent regions of the weld microstructure. TEM foils were machined from the top layer of the weld containing the remelted metal. They were treated with a dual jet polishing apparatus and solution of 60% perchloric acid and 99% acetic acid at temperature 13°C, voltage 70 V, and direct current 0.13 A within a time range from 2 to 10 s.

Orientation imaging microscopy (OIM) was applied in order to examine the relationship between morphology and crystal orientation in the weld microstructure (Refs. 38–40). Measurements were

based on an electron backscattering diffraction pattern (EBSP) consisting of sets of Kikuchi lines, which represent planes in the diffracting volume. The distance between lines is a function of the interplanar spacing. The lattice orientation can be detected from the geometrical orientation of the lines (Ref. 40). For this purpose, the SEM was equipped with an EBSP analyzer that was also used for phase identification. Ferrite and austenite were identified by a “confidence index” (not less than 0.6) of indexed EBSP. The SEM electron beam is at an angle of 70 deg to the direction of the sample normal. Measurements took place after the projection RD of the SEM electron beam on the sample plane was aligned with the apparent growth direction of clearly outlined dendrites or cells. Then RD points to the upper apparent direction of crystal growth. Statistically it has been found under such conditions the RD can deviate less than 5 deg from the real growth direction (Ref. 41). This can be used as estimate of error, which is considered to be not significant for the results obtained in this study. Single orientation measurements were carried out in tens of points along dendrites covering the whole grain area. For simplicity, only representative points are shown superimposed on the micrographs.

## Results

### Microstructure of Type 310S Laser Spot Welds

Figure 3 represents a fully austenitic microstructure of a pulse laser beam weld irradiated for 1 s. Epitaxial growth took place at the fusion boundary. It started with a planar solidification front that

**Table 3 — GTA Welding Conditions**

Voltage, V	12
Current, A	120
Welding speed, mm/s	3
Shielding gas	Ar
W-electrode diameter, mm	3

propagated into the weld before it broke down into cells. Cellular dendrites with primary and secondary dendrite arms are discernable in the bulk of the fusion zone. No ferrite was found in the intercellular or in the interdendritic regions, suggesting the austenitic solidification mode of this microstructure. Impurity segregation combined with a high weld restraint often results in hot cracking, as visible in Fig. 3B. Similar microstructure features were also revealed under 100- and 10-ms laser irradiation, as shown in Figs. 4 and 5. Reduction of the heat input caused dimming and flattening of the weld pool, resulting in very fine cells due to RS.

Segregation profiles of cellular and intercellular regions of a weld irradiated for 10 ms are presented in Fig. 6. In general the profiles of Cr, Ni, and Fe are rather flat across the cell. Intercellular regions are slightly depleted in Fe and enriched in Cr, whereas Ni segregation profile was unclear. These profiles confirm the austenitic solidification mode influenced by RS. Similar observations are reported elsewhere. It is well established that initial solidification starts with an epitaxial growth that is followed by competitive grain growth in the melt (Refs. 38, 39). Single-phase austenite solidification of Type 310S alloy results in a fully austenitic, crack-sensitive microstructure obtainable under different quenching methods from the melt during GTA welding

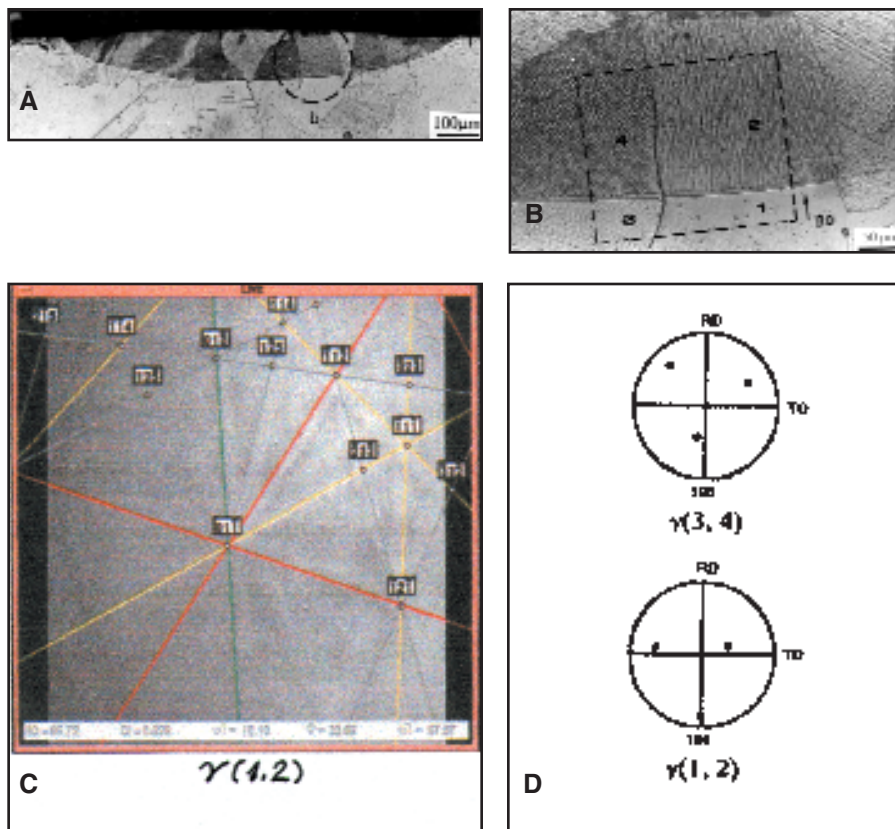


Fig. 4 — Microstructure orientation relationship of a 310S laser spot weld irradiated for 10 ms at a defocused distance of 10 mm. A — Vertical section; B — region examined using OIM; 1, 3 — partially melted grains; 2, 4 — weld metal grains; C — EBSD (for austenite hkl legend, see Fig. 8D); D — pole figures of corresponding grains.

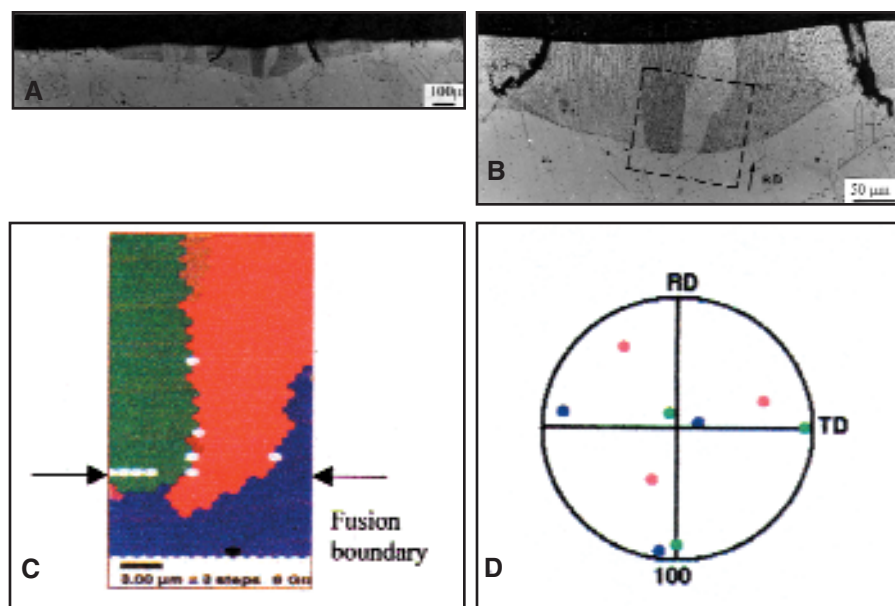


Fig. 5 — Microstructure orientation relationship of a 310S laser spot weld irradiated for 10 ms at a defocused distance of 15 mm. A — Vertical section; B — region examined using OIM; C — grain color map of the region framed in B; D — combined austenite pole figure.

(Refs. 28, 33), laser beam welding (Refs. 7, 23, 24, 32), electron beam welding (Refs. 26, 32, 34), and splat quenching (Ref. 22). Very low degree of segregation has been measured in high-energy-density welds (Refs. 22, 32).

It is well known that an approximate relationship exists between dendrite arm spacing and the cooling rate (Refs. 23, 43) and the latter is not constant for a given weld. The measured cell spacing was in the range from 1.7 to 6.3  $\mu\text{m}$ , as displayed in Table 2. It was found to correspond to a cooling rate on the order of  $4 \cdot 10^3$  to  $4 \cdot 10^5$   $^\circ\text{C/s}$ . Cooling rates of Type 310S alloy welds on the same order of  $1.9 \cdot 10^3$  to  $4.4 \cdot 10^5$   $^\circ\text{C/s}$  in electron beam welding as well as higher cooling rates from  $5 \cdot 10^4$  to  $5 \cdot 10^5$   $^\circ\text{C/s}$  in laser spot welding have been reported (Refs. 23, 26).

### Crystallographic Orientation of Type 310S Laser Spot Welds

The region framed in Fig. 4B of the 10-ms spot weld was investigated using OIM. Numbers 1 to 4 superimposed on the micrograph designate representative portions of two couples of neighboring grains where single orientation measurements were carried out. Figure 4C and D shows the EBSD results confirming the austenitic microstructure of grain couple  $\gamma(1, 2)$ , as well as corresponding (100) pole figures. Both the EBSD and the austenite  $\langle 100 \rangle_\gamma$  in the pole figure are identical for portions 1 and 2, confirming the epitaxial growth from the heat-affected zone (HAZ). Also,  $\langle 100 \rangle_\gamma$  is aligned in the apparent cell growth direction and is invariant along weld metal cells as well as over the entire partially melted grain. In addition, the epitaxial growth from the partially melted grain results in just one weld metal grain as visible in Fig. 4A and B. Similar results were obtained for the other grain couple  $\gamma(3, 4)$ . In this case  $\langle 100 \rangle_\gamma$  in the corresponding pole figure is not parallel to RD, which is aligned with the cell growth direction of grain couple  $\gamma(1, 2)$ .

Further results also confirmed that grain growth was epitaxial, and the  $\langle 100 \rangle_\gamma$  of the base grain was kept invariant along apparent cell growth direction throughout the new grain regardless of the direction of the temperature gradient. This is evident in Fig. 5C and D, where the fully austenitic microstructure of the region framed in Fig. 5B was confirmed by the EBSDs. The grain orientation is presented by both a grain color map and (100) pole figures. The  $\langle 100 \rangle_\gamma$  of the green and the blue grain are nearly identical or close to the cell growth direction, respectively,

1. To be read  $\langle 100 \rangle_\gamma$  in point 1 to 2.

that is presumed to be close to the direction of the temperature gradient. In contrast, the orientation  $\langle 100 \rangle_\gamma$  of the pink grain is far from the cell growth direction. Nevertheless, the pink grain  $\langle 100 \rangle_\gamma$  does not change along cells from the fusion boundary to the weld pool surface, forming just one columnar grain. The white spots in the color map are due to some surface defects in the sample.

In addition, grain boundaries can be distinguished by applying a chemical etchant that attacks grain boundaries preferentially. Some etchants may also attack grains of different orientation at different rates, creating topological contrast depending on lattice orientation. Generally, it is the crystallographic orientation that reveals the morphology (Ref. 38). From the micrographs in Figs. 4A and 5A, it can be seen that the weld metal grains differ significantly, contrasting with each other, and that the contrast is kept constant over the entire grain, thus confirming constant crystallographic orientation of each single grain.

### Microstructure of Type 304 GTA Welds

The weld microstructure revealed predominantly vermicular and lacy ferrite as well as acicular ferrite in an austenitic matrix, as seen in Fig. 7A. These ferrite morphologies were attributed to a preferential FA solidification accompanied by F solidification, presumably due to a local enrichment in the weld pool followed by  $\delta$ - $\gamma$  transformation in solid state (Refs. 1, 6, 16). The ferrite morphologies could also be due to local fluctuations of growth rates near fusion boundaries. In the case of a very slow solidification, microstructure due to type F solidification is likely to be observed, while type FA solidification occurs at slightly faster growth rates. The grain substructure consists of coarse dendrites with primary arm spacing of approximately 16 mm developed under an estimated cooling rate of 115°C/s. A significant degree of Cr and Ni segregation was revealed across dendrites (Ref. 47).

### Crystallographic Orientation of Type 304 GTA Welds

A microstructure orientation relationship of the area framed in Fig. 7A is displayed in Fig. 7B and C. Representative points 1 to 4 are superimposed on the SEM micrograph. Points 1, 3, and 4 are indicative of austenite while point 2 indicates retained ferrite. Heat-affected zone austenite  $\langle 100 \rangle_\gamma$ -1 is not parallel to the dendrite growth direction RD, whereas ferrite  $\langle 100 \rangle_\delta$ -2 is along it. A Kurdumov-Sachs (K-S) orientation relationship  $\{111\}_\gamma \parallel \{110\}_\delta$  and  $\langle 110 \rangle_\gamma \parallel \langle 111 \rangle_\delta$  (Ref. 46) was established between base

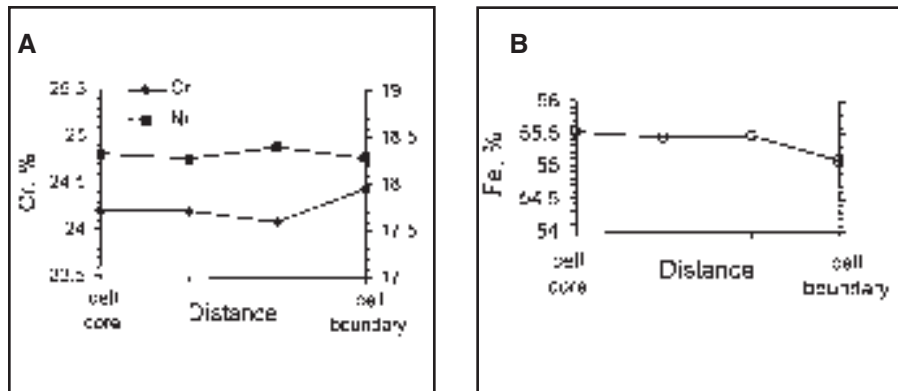


Fig. 6 — TEM EDS segregation profiles in Type 310S laser spot weld irradiated for 10 ms at a defocused distance of 10 mm. A — Cr and Ni profile; B — Fe profile.

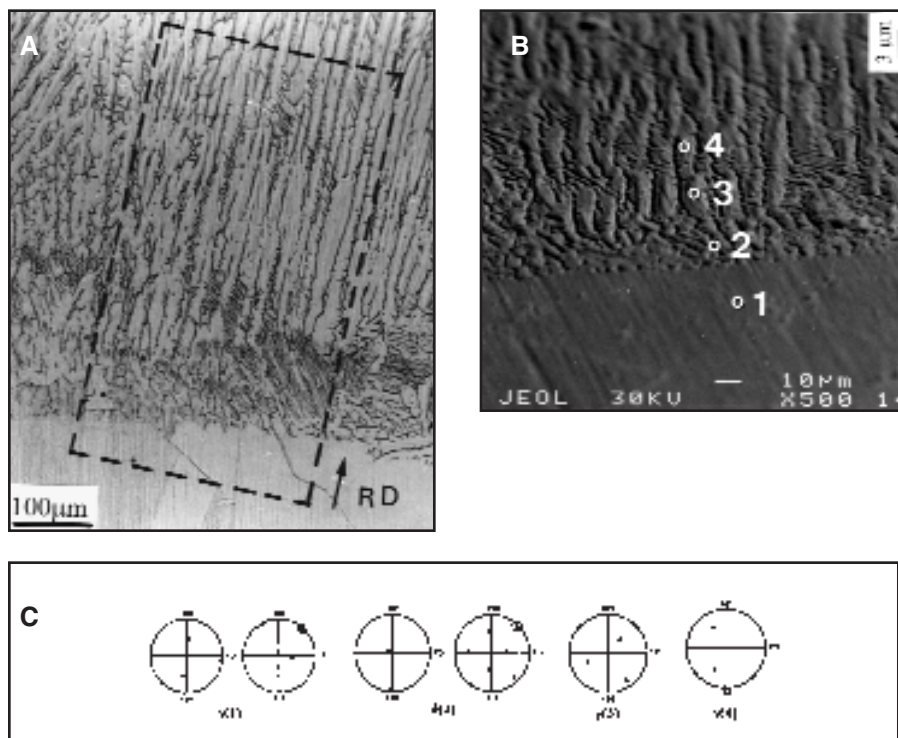


Fig. 7 — Microstructure orientation relationship of a 304 GTA weld. A — Microstructure at the weld interface; B — SEM micrograph: 1 to 4, locations examined using OIM; 1, 3, and 4, austenite; 2, ferrite; C — pole figures of corresponding points.

metal austenite  $\gamma$ (1) and weld metal ferrite  $\delta$ (2), confirming epitaxial growth of primary ferritic dendrites during solidification.  $\langle 100 \rangle_\gamma$ -3 and  $\langle 100 \rangle_\gamma$ -4 in the weld metal were different and were found to deviate not only from the dendrite growth direction RD but also from  $\langle 100 \rangle_\gamma$ -1 as well. Moreover, various  $\langle 100 \rangle_\gamma$  were observed between points 3 and 4 as well as beyond point 4 along the dendrite, which are not displayed in Fig. 7C.

### Microstructure of Type 304 Laser Spot Welds

The microstructure of a weld produced by 1000-ms laser irradiation is shown in Fig. 8A. Darker and lighter etching

patches reveal duplex cellular microstructure. Varying ferrite volumes and morphologies, such as vermicular, lacy, acicular, and globular ferrite, were observed in the fusion zone. They are related to FA or F solidification and subsequent incomplete  $\delta$ - $\gamma$  transformation (Refs. 6, 7, 15, 16, 23, 24). When laser irradiation was reduced to 100, 10, 5, and 1 ms, the decrease in the amount of ferrite was accompanied by a transition to a nearly fully austenitic microstructure as visible in the micrographs in Figs. 9–12. These microstructures are likely to be due to a mixed solidification mode of FA plus AF, or A plus FA, or even E as noted in previous works (Refs. 7, 23, 24). Segregation profiles were taken across laser beam weld cells irradi-

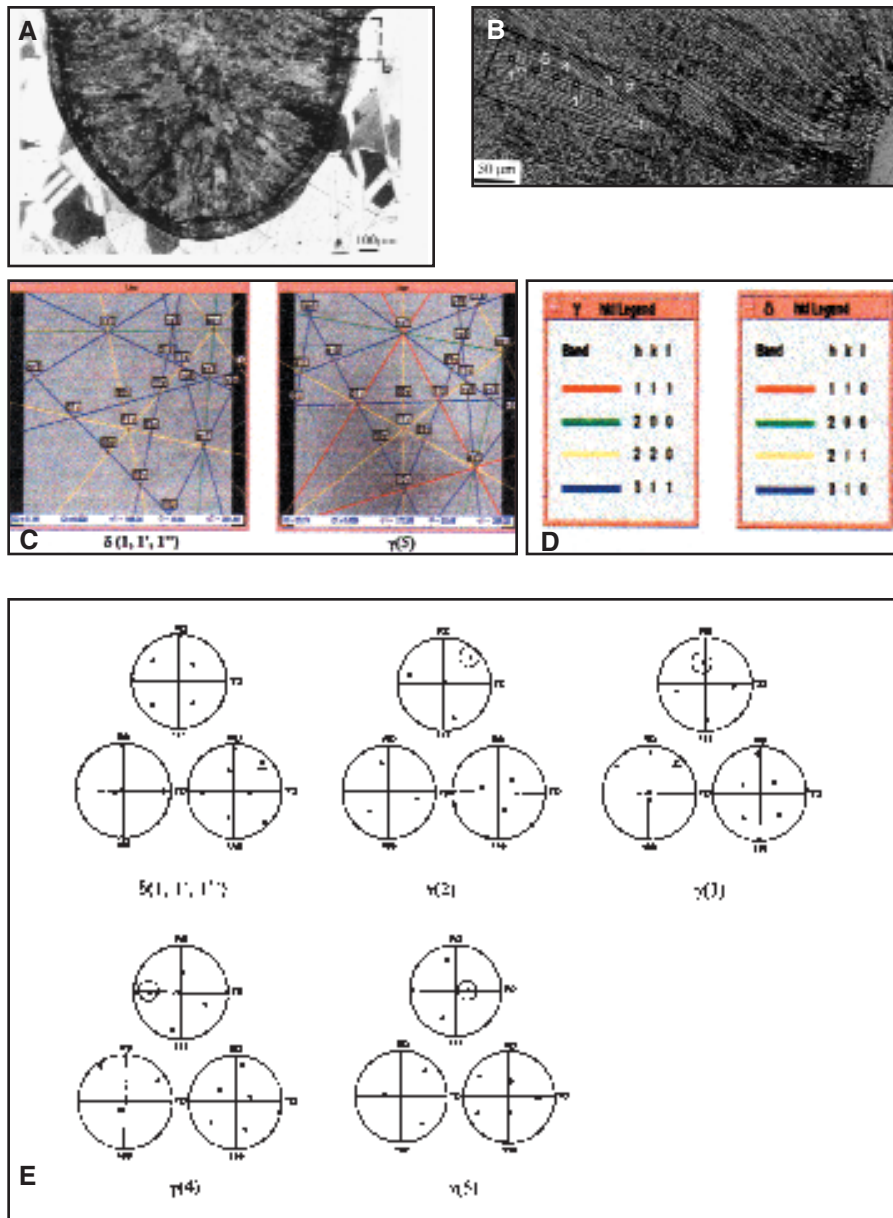


Fig. 8 — Microstructure orientation relationship of a 304 laser spot weld irradiated for 1000 ms at a defocused distance of 10 mm: A — vertical section; B — region examined using OIM; C — EBSPs of ferrite and austenite at corresponding points; D — ferrite and austenite hkl legend; E — pole figures taken at corresponding points.

ated for 10 and 5 ms; however, the findings were unclear and need further research. The reduction of laser irradiation from 1000 to 5 ms resulted in an extremely low cell spacing, decreasing from 5 to 0.9 mm, due to an estimated cooling rate increase from  $6.10^3$  °C/s to  $5.10^6$  °C/s according to Table 2. These values are consistent with the cooling rates reported earlier (Refs. 7, 23, 27).

It can be seen in the microstructures shown in Figs. 9A–12A that the number of new austenite grains at the fusion boundary increased as compared to that of the partially melted grains. This phenomenon was also noted in other 304 laser beam

welds performed under various welding conditions but not presented here. In contrast, just one new grain was found to grow epitaxially from each partially melted grain in any of the 310S laser beam weld metals as seen in Figs. 3–5. Further, although a dramatic reduction in the amount of ferrite was found in the 304 weld metals, no cracking was established in the duplex structures or in the fully austenitic regions of the fusion zone. Since hot cracking is composition and weld-restraint dependent (Ref. 13), it is obvious from this finding that a fully austenitic microstructure does not necessarily have to be prone to cracking, which is in agree-

ment with the results reported in Ref. 7. However, this finding is in contrast to those of other studies on 304 laser beam and electron beam welds where hot cracks have been observed (Refs. 23, 25).

### Crystallographic Orientation of Type 304 Laser Spot Welds

An optical micrograph of a region examined using OIM is shown in Fig. 8B. Points 1 to 5 are superimposed on a selected elongated cell along the cell growth direction. The EBSPs in Fig. 8C, taken in points 1, 1', and 1'', were identical. With the help of the ferrite or austenite hkl legends displayed in Fig. 8D, the above EBSPs revealed δ-ferrite, while those taken in points 2 to 5 indicated austenite phases. According to the pole figures in Fig. 8E, ferrite  $\langle 100 \rangle_\delta$  is parallel to the cell growth direction. Various  $\langle 100 \rangle_\gamma$ -2-5 exist along the cell and most of them are not aligned in the direction of the elongated cell growth. K-S orientation relationships hold between the ferrite δ(1, 1', 1'') and the austenite phases γ(2) to γ(5) as shown by means of the circled reflectors. For clarity, the corresponding  $\langle 110 \rangle_\delta$  reflectors are not circled. Also, the Bain orientation relationship  $\langle 100 \rangle_\gamma \parallel \langle 110 \rangle_\delta$  (Ref. 46) is established between ferrite δ(1, 1', 1'') and austenite γ(3), as indicated by the corresponding underlined reflectors.

After reduction of laser irradiation from 100 to 1 ms, the weld microstructures were confirmed by EBSPs, not shown here, as being nearly fully austenitic. An SEM micrograph of a region in Fig. 9A of a 10-ms irradiated weld is shown in Fig. 9B. No ferrite was found present even after very slight etching in order to reveal the microstructure. Because the weld metal is fully austenitic, there is no means to determine orientation relationship between the ferrite and austenite. However, in Fig. 9C, HAZ grain austenite  $\langle 100 \rangle_\gamma$ -1 and weld metal austenite  $\langle 100 \rangle_\gamma$ -2-3 were found to deviate from the cell growth direction, whereas  $\langle 100 \rangle_\gamma$ -4 was nearly parallel to it. A microstructure orientation relationship established for a laser beam weld irradiated for 10 ms at a defocused distance of 20 mm is presented in Fig. 10. A short epitaxial austenite growth, as evidenced by the nearly identical HAZ  $\langle 100 \rangle_\gamma$ -1 and weld metal  $\langle 100 \rangle_\gamma$ -2, took place near the fusion boundary in a direction different from that of the elongated cell. Further growth of austenite, however, was found to be close to the cell growth direction according to the pole figure  $\langle 100 \rangle_\gamma$ -3, as well as  $\langle 100 \rangle_\gamma$ -4. Figure 11 demonstrates a spot weld irradiated for 20 ms at a defocused distance of 20 mm. The microstructure was nearly fully austenitic.

Figure 11B and C reveals cellular dendrites growing in different directions in the new red austenite grain  $\gamma(3)$ . Also, austenite orientations of the HAZ grains  $\gamma(1, 2)$  and the new grain  $\gamma(3)$  were not identical. These findings were not observed in type 310S weld metal, where cell growth occurred in  $\langle 100 \rangle_{\gamma}$  which is identical for both the substrate austenite and the new grain austenite.

An increasing number of new grains, as compared to that of the HAZ grains, is established at the fusion boundary in Fig. 11C. Figure 11D presents a color map of the region “d” framed in Fig. 11A. Two partially melted grains and many new austenite grains in the fusion zone, growing seemingly epitaxially, were identified within the total number of 75 grains. Most of the new grains have  $\langle 100 \rangle_{\gamma}$  different from that of the HAZ grains. Figure 12 shows a microstructure orientation relationship of a laser beam weld irradiated for 5 ms at a defocused distance of 20 mm. In Fig. 12C, the fusion boundary separates a green-colored, partially melted grain from several differently colored new grains with a total number of 10. The new grains seem to grow epitaxially from the green grain. However, it is evident from the pole figure in Fig. 12D that  $\langle 100 \rangle_{\gamma}$  of the HAZ grain differs from those of the new grains. Also, any given  $\langle 100 \rangle_{\gamma}$  is not parallel to the RD, which is aligned with the clearly outlined cells shown in Fig. 12B.

## Discussion

Except for some boundary migration after solidification is completed, Type 310S alloy experiences no transformation on cooling (Refs. 1, 2, 4, 7, 22–24, 26). Therefore, the origin of this microstructure is easy to understand. On the other hand, RS of Type 304 alloy under laser beam welding might create some difficulties in understanding the mechanism of weld microstructure formation. The results of this study are easy to explain by considering the following: 1) direction of the temperature gradient, 2) apparent direction of primary cell or dendrite growth, 3) easy-growth direction  $\langle 100 \rangle_{\delta}$  of ferrite, 4) easy-growth direction  $\langle 100 \rangle_{\gamma}$  of austenite, 5) upper direction RD (of SEM beam projection on the sample plane), which is aligned in the apparent direction of cell or dendrite growth.

### Austenite $\langle 100 \rangle$ Variation in Dendrite or Cell Growth Direction

A common feature of both 304 GTA and laser beam weld microstructures is the presence of numerous  $\langle 100 \rangle_{\gamma}$  along elongated dendrites or cells. It is obvious that the GTA weld shown in Fig. 7 undergoes a

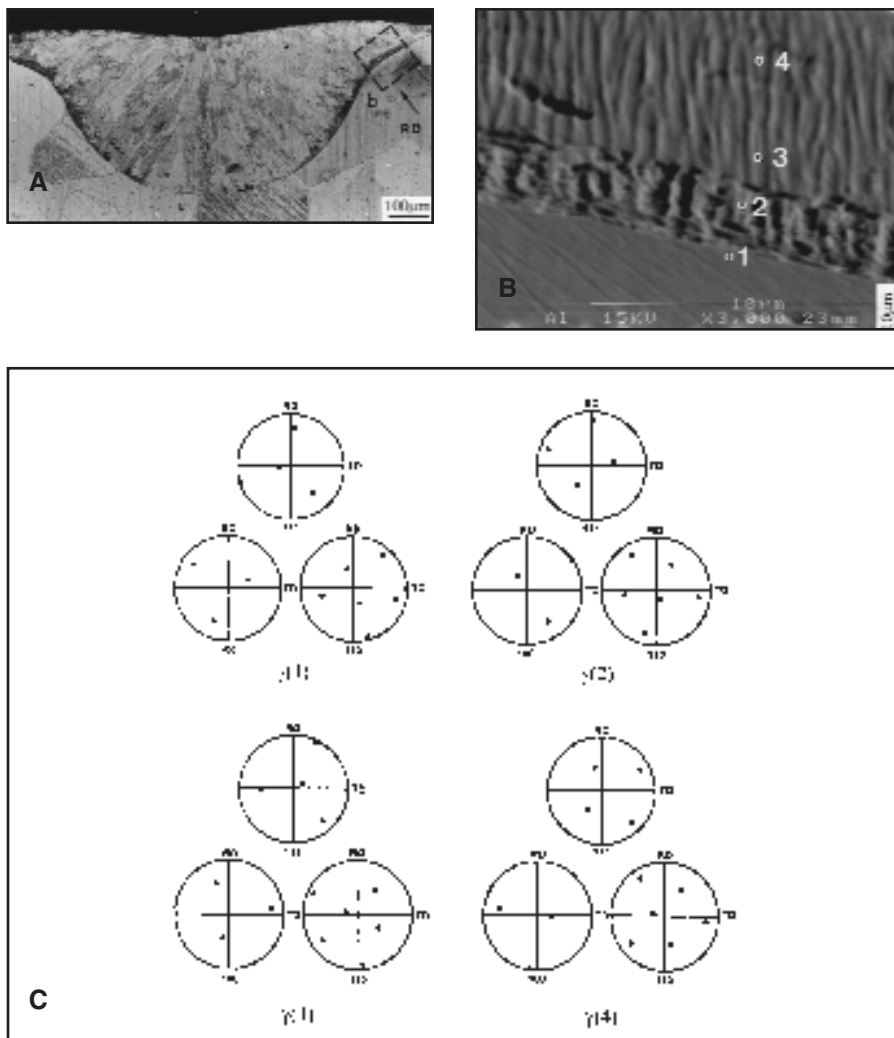


Fig. 9 — Microstructure orientation relationship of a 304 laser spot weld irradiated for 10 ms at a defocused distance of 100 mm: A — vertical section; B — SEM microstructure of a region examined using OIM; C — pole figures taken at corresponding points.

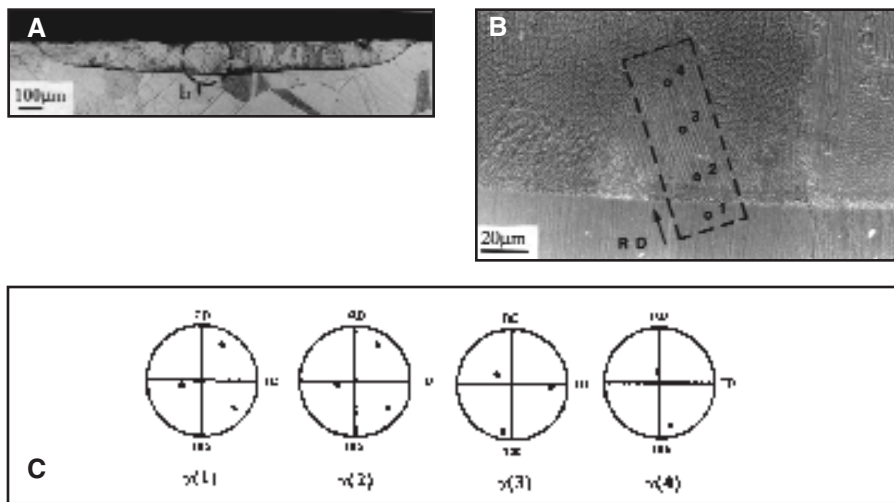


Fig. 10 — Microstructure orientation relationship of a 304 laser spot weld irradiated for 10 ms at a defocused distance of 20 mm: A — vertical section; B — optical micrograph of a region examined using OIM; C — pole figures taken at corresponding points.

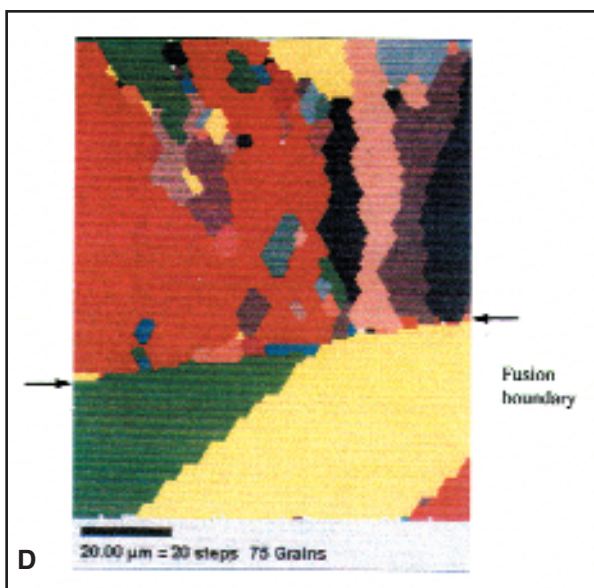
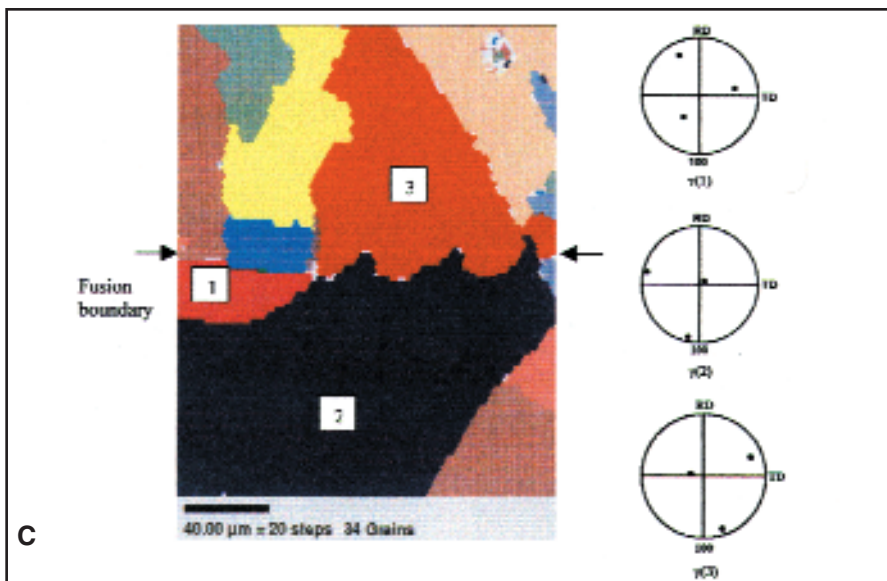
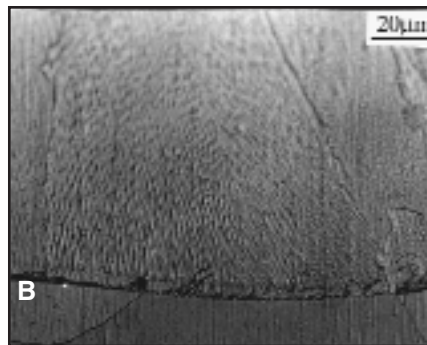
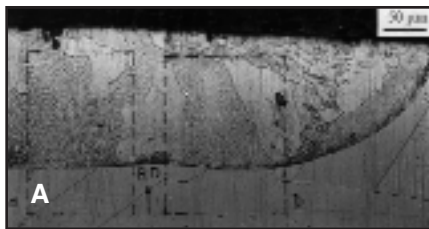


Fig. 11 — Microstructure orientation relationship of a 304 laser spot weld irradiated for 20 ms at a defocused distance of 20 mm: A, B — optical micrograph; C — grain color map of the region framed in A and austenite pole figures at corresponding grains; D — grain color map of the region framed in A showing new grains in the weld metal.

solid-state  $\delta$ - $\gamma$  transformation following FA and F solidification mode. Eutectic austenite with  $\langle 100 \rangle_\gamma$  in the dendrite growth direction or peritectic austenite with  $\langle 100 \rangle_\gamma$  different from the dendrite growth direction might form in the last liquid to solidify, if the solidification is of FA mode (Refs. 29, 30). Provided the melt so-

lidifies in F mode, austenite nucleates in the interdendritic regions, holding a K-S orientation relationship with ferrite. Thus, based on their origin, there are various austenite phases that might play a significant role during  $\delta$ - $\gamma$  transformation. The most favorably oriented austenite phase, whose  $\langle 100 \rangle_\gamma$  is closest to the temporal

direction of the temperature gradient, propagates into the ferrite, accomplishing the transformation.

It was found in Fig. 7C that normally the  $\langle 100 \rangle_\delta$  of ferrite is aligned in the primary dendrite growth direction. If base metal  $\langle 100 \rangle_{\gamma-1}$  varies widely from it, an epitaxial growth from the base metal during  $\delta$ - $\gamma$  transformation becomes extremely difficult. Above growth might be suppressed, as in the case of Figs. 7C and 9C, or it might be obstructed and stopped within a very short distance across the fusion boundary, as found in Fig. 10C, Fig. 12C, and in a previous work (Ref. 47). Instead, at that instant, a more favorably oriented weld metal austenite becomes more active, performing the transformation. As a result, weld metal austenite  $\langle 100 \rangle_\gamma$  varies along dendrites beyond the epitaxial growth range. The variations in  $\langle 100 \rangle_\gamma$  are inherent for the  $\delta$ - $\gamma$  transformation because of the great number of habit planes (24), which could be selected by the austenite in order to favor its growth direction and, hence, to ease its growth depending on the direction of the temperature gradient. Conversely, when base metal  $\langle 100 \rangle_\gamma$  is close to the dendrite growth direction, an epitaxial austenite growth takes place from the HAZ across the fusion boundary within a significant range along the primary ferritic dendrite. This growth becomes interrupted when a critical change of the temperature gradient direction occurs. This is not observed in Type 310S welds where, after solidification of A mode,  $\langle 100 \rangle_\gamma$  coincides with both the  $\langle 100 \rangle$  of the substrate austenite and the cell growth direction.

### Origin of the New Weld-Metal Grains

The origin of the new grains could be interpreted considering the mechanism of  $\delta$ - $\gamma$  solid-state transformation. Under the cooling rates encountered in arc welding,  $\delta$ - $\gamma$  transformation is diffusion-controlled (Refs. 7, 13-16, 22, 25, 28, 32, 33). Rapid cooling from the molten state is reported to provide a massive transformation (Refs. 28-32, 53, 54), although its features appear to be still controversial (Refs. 29, 32, 55-59). The existing cells of the 304 laser beam weld metal observed in this study suggest that partitioning under laser beam welding conditions is not fully suppressed and provide an evidence for some degree of diffusion. Thus, the transformation is due to an advancing  $\delta$ - $\gamma$  interface into the ferrite phase. Since the direction of the temperature gradient changes during welding, the advancing austenite phases tend to orient their easy growth direction  $\langle 100 \rangle_\gamma$  toward the direction of the temperature gradient. It is well known that normally there is a deviation between these two directions, which is time and po-

sition dependent (Refs. 42, 43, 60). When the magnitude of deviation exceeds a presumably critical value, the current growth direction of the austenite becomes less favorable and a shift takes place to a new austenite phase with a preferable growth direction, closer to the momentary direction of the temperature gradient. Within the short time range between two subsequent changes of the easy growth direction  $\langle 100 \rangle_\gamma$  the austenite phase forms a fine new grain. After subsequent  $\langle 100 \rangle_\gamma$  changes, a multitude of fine new grains forms at the fusion boundary just above the single, partially melted grain. In contrast, during primary solidification with austenite, as in the case of Type 310S, weld epitaxial growth takes place from the single, partially melted grain, which performs the only nucleation phase. This growth results in just one new weld metal grain, situated above the substrate grain.

There are two points to be considered here. First, grains are three-dimensional but the data interpreted in this study are two-dimensional in nature. Also, the depth of the HAZ grains, where the data were taken, is not known. Thus, one could not exclude the probability that there might be a higher-than-one number of HAZ grains situated under the partially melted grain and their epitaxial growth might have contributed to the number increase of new grains. However, since the HAZ grains are much larger than the new grains and their number around the fusion zone is limited, as seen in Figs. 9–12, the effect of such contribution is unlikely to be significant. Second, the HAZ green grain shown in Fig. 12C and D has a  $\langle 100 \rangle_\gamma$  which is rotated to roughly 45 deg relative to RD, so it should have chosen two  $\langle 100 \rangle_\gamma$  growth directions. Being not in an orientation of preferred growth, this grain is likely to be eliminated by competitive growth not far from the fusion boundary. However, its contribution to the number increase of new grains does not seem to be significant, as seen in Fig. 12C and D, where the  $\langle 100 \rangle_\gamma$  of several grains is identified.

Taking into account the above considerations, it can be concluded that the austenitic microstructure of Type 304 laser beam welds obtained under irradiation for 1 s to 1 ms is a result of ferrite, not austenite, solidification as a leading phase followed by  $\delta$ - $\gamma$  transformation. It is believed that ferrite of lower-than-normal  $Cr_{eq}/Ni_{eq}$  ratios forms due to undercooling during RS and, stimulated by reduced compositional differences, it readily transforms to austenite (Ref. 49). Thus, it is obvious the cooling rate experienced by the weld metal in this study has been less than the critical one necessary to achieve melt undercooling in order to shift solidification to primary austenitic.

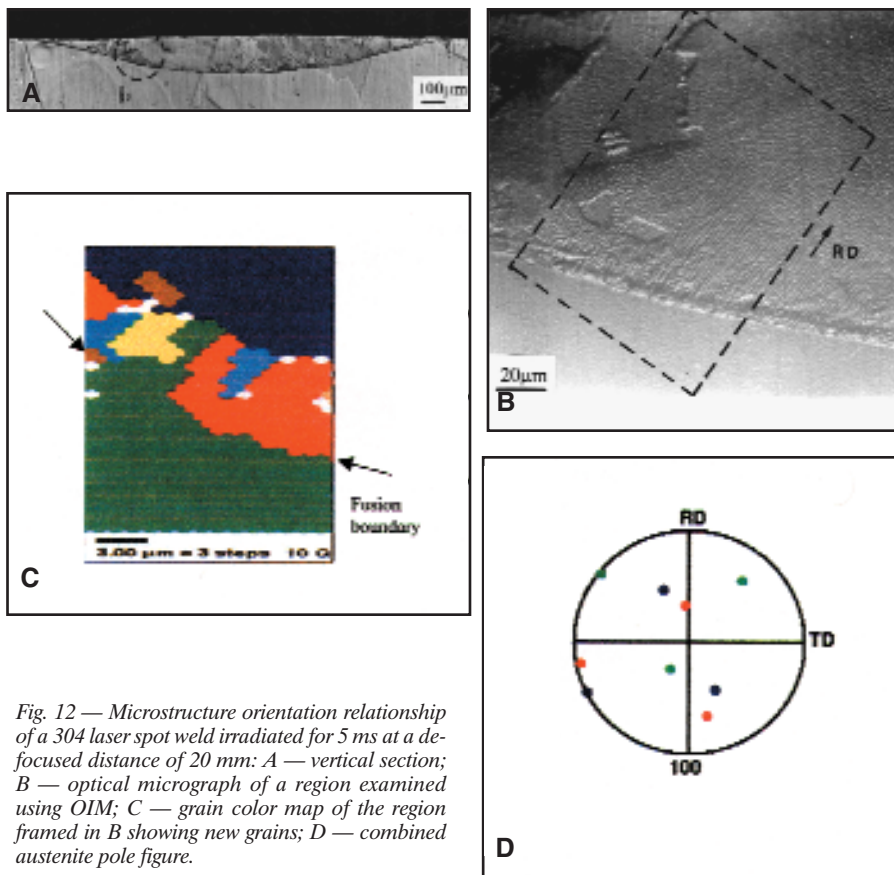


Fig. 12 — Microstructure orientation relationship of a 304 laser spot weld irradiated for 5 ms at a defocused distance of 20 mm: A — vertical section; B — optical micrograph of a region examined using OIM; C — grain color map of the region framed in B showing new grains; D — combined austenite pole figure.

## Conclusions

1) A fully austenitic microstructure was observed in Type 310S laser beam welds. Cell spacing decreased significantly due to a rapid solidification. Epitaxial grain growth taking place in the  $\langle 100 \rangle_\gamma$  of the base grain was aligned with the cell growth direction and resulted in just one columnar weld metal grain. Segregation profiles across solidification cells were nearly flat; nevertheless, significant hot cracks were found in the fusion zone.

2) Vermicular, lacy, and acicular ferrite in an austenitic matrix was observed in the GTA weld metal microstructure, attributed to FA and F solidification mode followed by a solid state  $\delta$ - $\gamma$  transformation. Numerous  $\langle 100 \rangle_\gamma$  orientations of austenite existed along primary dendrite.

3) A transition from austenite plus ferrite to nearly fully austenitic weld metal was observed in Type 304 laser beam welds. Many small new grains were found to grow apparently epitaxially from one partially melted grain. In most cases, the  $\langle 100 \rangle_\gamma$  of the substrate austenite and the new grain austenite were different and not aligned with the direction of primary cell growth. Numerous  $\langle 100 \rangle_\gamma$  orientations existed along primary cells. This microstructure was attributed to originate from  $\delta$ - $\gamma$  transformation following primary ferrite solidi-

fication mode. Although fully austenitic, the microstructure was crack-free.

4) The following criteria are recommended for identification of fully austenitic weld microstructure (if ferrite volume fraction is extremely low or there is a lack of it), formed as a result of primary ferrite solidification and solid-state  $\delta$ - $\gamma$  transformation:

- Austenite  $\langle 100 \rangle_\gamma$  varying along cell growth direction;
- Presence of many small new grains that seem to grow epitaxially from one partially melted grain.

5) The cooling rate experienced by the 304 laser beam weld metal was less than the critical one necessary to cause undercooling that results in a shift of the solidification mode from primary ferritic to primary austenitic.

6) The cells observed in the 304 laser beam weld metal suggest that partitioning under laser beam welding conditions is not fully suppressed and provide an evidence for some degree of diffusion, thus excluding the occurrence of massive solidification or massive transformation of the ferrite or austenite phase.

### Acknowledgments

The authors wish to thank Dr. K. Ikeuchi, professor of JWRI of Osaka Uni-

versity, for his assistance in operating TEM and EDS of TEM.

### References

1. Suutala, N., Takalo, T., and Moisio, T. 1979. The relationship between solidification and microstructure in austenitic and austenitic-ferritic stainless steel welds. *Metallurgical Transactions A* 10A: 512–514.
2. Takalo, T., Suutala, N., and Moisio, T. Austenitic solidification mode in austenitic stainless steel welds. 1979. *Metallurgical Transactions A* 10A(8): 1173–1181.
3. Suutala, N., Takalo, T., and Moisio, T. 1979. Single phase ferritic solidification mode in austenitic-ferritic stainless steel welds. *Metallurgical Transactions* 10A(8): 1183–1190.
4. Katayama, S., Fujimoto, T., and Matsunawa, A. 1985. Correlation among solidification process, microstructure, microsegregation and solidification cracking susceptibility in stainless steel weld metals. *Transactions of the JWRI* (14)1: 123–138.
5. Lippold, J., and Savage, W. 1980. Solidification of austenitic stainless steel weldments: Part 2 — The effect of alloy composition on ferrite morphology. *Welding Journal* 59(2): 48-s to 58-s.
6. David, S. 1981. Ferrite morphology and variations in ferrite content in austenitic stainless steel welds. *Welding Journal* 60(4): 63-s to 71-s.
7. David, S., Vitek, J., and Hebble, T. 1987. Effect of rapid solidification on stainless steel weld metal. Microstructures and its implications on the Schaeffler diagram. *Welding Journal* 66(10): 289-s to 300-s.
8. Hull F. 1967. Effect of delta ferrite on the hot cracking of stainless steel. *Welding Journal* 46(9): 399-s to 409-s.
9. Arata, Y., Matsuda, F., and Sruwatari, S. 1974. Vareststraint test for solidification crack susceptibility in weld metal of austenitic stainless steels. *Transactions of the JWRI* (3)1: 79–88.
10. Lundin, C., DeLong, W., and Spond, D. 1975. Ferrite fissuring-relationship in austenitic stainless steels weld metals. *Welding Journal* 54(8): 241-s to 246-s.
11. Arata, Y., Matsuda, F., and Katayama, S. 1976. Solidification crack susceptibility in weld metals of fully austenitic stainless steels. *Transactions of the JWRI* (5)2: 35–51.
12. Brooks, J., and Lambert, F. 1978. The effect of P, S and ferrite content on the weld cracking of Type 309 stainless steel. *Welding Journal* 57(5): 139-s to 143-s.
13. Lippold, J., and Savage, W. 1982. Solidification of austenitic stainless steel weldments. Part 3 — The effect of the solidification behavior on hot cracking susceptibility. *Welding Journal* 61(12): 388-s to 396-s.
14. Brooks, J., Thomson, A., and Williams, J. 1984. A fundamental study on the beneficial effects of delta ferrite in reducing weld cracking. *Welding Journal* 63(3): 71-s to 83-s.
15. Cieslak, M., Ritter, A., and Savage, W. 1982. Solidification cracking and analytical electron microscopy of austenitic stainless steel weld metals. *Welding Journal* 61(1): 1-s to 8-s.
16. Suutala, N. 1983. Effect of solidification conditions on the solidification mode in austenitic stainless steel. *Metallurgical Transactions A* 14A(2): 191–197.
17. Suutala, N. 1982. Effect of manganese and nitrogen on the solidification mode in austenitic stainless steel welds. *Metallurgical Transactions A* 13A(12): 2121–2130.
18. Hammar, O., and Svenson, U. 1979. Influence of steel composition on segregation and microstructure during solidification of austenitic stainless steels. *Solidification and Casting of Metals*. London, U.K.: The Metals Society, pp. 401–410.
19. Shaeffler, A. 1949. Constitution diagram of stainless steel weld metal. *Metal Progress* 56(5): 680–680b.
20. DeLong, W. 1974. Ferrite in austenitic stainless steel metal. *Welding Journal* 53(7): 273-s to 286-s.
21. Leone, G., and Kerr, H. 1982. The ferrite to austenite transformation in stainless steels. *Welding Journal* 61(1): 13-s to 21-s.
22. Vitek, J., Dasgupta, A., and David, S. 1983. Microstructural modification of austenitic stainless steel by rapid solidification. *Metallurgical Transactions A* 14A: 1833–1841.
23. Katayama, S., and Matsunawa, A. 1984. Solidification microstructure of laser welded stainless steels. *Proc. of Mater. Processing Symposium*, Laser Inst. of America. ICALCO, Vol. 44, pp. 60–67.
24. Katayama, S., and Matsunawa, A. 1985. Solidification behavior and microstructural characteristics of pulsed and continuous laser welded stainless steels. *Proc. of Mater. Processing Symposium*, Laser Inst. of America. ICALCO, Vol. 45, pp. 19–25.
25. Lippold, J. 1985. Centerline cracking in deep penetration electron beam welds in Type 304L stainless steel. *Welding Journal* 64(5): 127-s to 136-s.
26. Elmer, J., Allen, S., and Eagar, T. 1989. Microstructural development during solidification of stainless steel alloy. *Metallurgical Transactions A* 20A(10): 2117–2131.
27. Venkataraman, S., and Devletian, J. 1988. Rapid solidification of stainless steel by capacitor discharge welding. *Welding Journal* 67(6): 111-s to 118-s.
28. Kou, S., and Le, Y. 1982. The effect of quenching on the solidification structure and transformation behaviour of stainless steel welds. *Metallurgical Transactions A* 13A: 1141–1152.
29. Inoue, H., Koseki, T., Ohkita, S., and Tanaka 1995. Effect of solidification on subsequent ferrite to austenite massive transformation in an austenitic stainless steel weld metal. *ISIJ International* 35(10): 1248–1257.
30. Inoue, H., Koseki, T., Ohkita, S., and Tanaka, T. 1996. Effect of solidification and subsequent ferrite morphologies in austenitic stainless steel welds. IHW Document IX-1835-96.
31. Mehrabian, R. 1982. Rapid solidification. *International Metals Reviews* 27(4): 185–207.
32. Brooks, J., Baskes M., and Greulich, F. 1991. Solidification modeling and solid state transformations in high energy density stainless steel welds. *Metallurgical Transactions A* 22A(4): 915–926.
33. Bhadeshia, H. K. D. H., David, S., and Vitek, J. 1991. Solidification sequences in stainless steel dissimilar alloy. *Materials Science and Technology* 7(1): 50–60.
34. Tsukamoto, S., Harada, H., and Bhadeshia, H. K. D. H. 1994. Metastable phase solidification in electron beam welding of dissimilar stainless steels. *Materials Science and Engineering A* 178: 189–194.
35. Fukumoto, S., and Kurz, W. 1997. The  $\delta$  to  $\gamma$  transition in Fe-Cr-Ni alloys during laser treatment. *ISIJ International* 37(7): 677–684.
36. Fukumoto, S., and Kurz, W. 1998. Prediction of the  $\delta$  to  $\gamma$  transition in austenitic stainless steel during laser treatment. *ISIJ International* 38(1): 71–77.
37. Fukumoto, S., and Kurz, W. 1997. Solidification phase and microstructure selection maps for Fe-Cr-Ni alloys. *ISIJ International* 39(12): 1270–1279.
38. Wright, S. 1993 A review of automated orientation imaging microscopy. *Journal of Computer Assisted Microscopy* 5(3): 207–221.
39. Dingley, D., and Randle, V. 1982. Review microtexture determination by electron back-scatter diffraction. *Journal of Materials Science* 27: 4545–4566.
40. Adams, B., Wright, S., and Kunze, K. 1993. Orientation imaging: the emergence of a new microscopy. *Metallurgical Transactions A* 24A(4): 819–831.
41. Yang, J., and Bhadeshia, H. K. D. K. 1989. Orientation relationships between adjacent plates of acicular ferrite in steel weld deposits. *Materials Science and Technology*, (5)1: 93–97.
42. Savage, W., Lundin, C., and Aronson, A. 1965. Weld metal solidification mechanics. *Welding Journal* 44(10): 433-s to 442-s.
43. Savage, W., and Aronson, A. 1966. Preferred orientation in the weld fusion zone. *Welding Journal* 45(11): 497-s to 503-s.
44. Flemmings, M. 1974. *Solidification Processing*. New York, N.Y.: McGraw-Hill Book Co., pp. 146–154.
45. David, S., Goodwin, G., and Braski, D. 1979. Solidification behavior of austenitic stainless steel filler metals. *Welding Journal* 59(11): 330-s to 336-s.
46. Cahn, R., and Haasen, P. 1983. *Physical Metallurgy*, 3rd ed. Amsterdam, The Netherlands: North Holland Physics Publishing, p. 1037.
47. Iamboliev, T., Katayama, S., and Matsunawa, A. 1997. Ferrite and austenite origin in a weld of a cast austenitic stainless steel type 18/8. *Proc. of Int. Congress Mechanical Engineering Technologies*. Ed. D. Butchkov, Vol. 3, pp. 25–34, Sofia NTS Press (in Bulgarian).
48. Iamboliev, T., Katayama, S., and Matsunawa, A. 1998. Phase formation under normal and rapid solidification in austenitic stainless steel welds. *Proc. of Int. Symposium Pipeline Welding '98*. Eds. B. Eryurek, O. Eti, C. Odabash, and A. Sevuk. Istanbul, Turkey: ITU Press, pp. 117–124.
49. Katayama, S., Iamboliev, T., and Matsunawa, A. 1998. Formation mechanism of rapidly quenched microstructure of laser weld metals austenitic stainless steels. *Proc. of the 51st Int. Conf. on Trends in Welding Research*. Eds. J. Vitek, S. David, J. Johnson, B. Smartt, and T. DebRoy. Callaway Gardens Resort, Pine Mountain, Ga., pp. 93–98.
50. Iamboliev, T., Katayama, S., and Mat-

sunawa, A. 1998. Mechanism of microstructure formation in pulse laser stainless steel welds. *Proc. of the Int. Symp. Welding on the Threshold of 21st Century*. Ed. A. Zhelev. Sozopol, Bulgaria, pp. 273–280.

51. Iamboliev, T., Katayama, S., and Matsunawa, A. 2000. Microstructure of GTAW and laser stainless steel welds. *Proc. of the Int. Conf. Welding & Joining. New Materials & New Perspectives*, Ed. A. Stern. Israel, pp. 83–85.

52. Iamboliev, T., Katayama, S., and Matsunawa, A. 2001. Criteria for solidification modes in stainless steel laser welds. *Proc. of the 4th European Conf. Eurojoin 4*. Eds. Z. Kozuh, and S. Kral. Dubrovnik. Cavtat, pp. 86–92.

53. Suutala, N., Takalo, T., and Moisiso, T.

1981. Technical note: Comment on the transformation  $\delta$ - $\gamma$  by massive mechanism in austenitic stainless steel. *Welding Journal* 61(5): 92-s to 93-s.

54. Lyman, C. 1979. Analytical electron microscopy of stainless steel weld metal. *Welding Journal* 59(7): 189–194.

55. Massalski, T. 1984. Distinguishing features of massive transformation. *Metallurgical Transactions A* 15A(3): 421–425.

56. Singh, J., Purdy, G., and Weatherly, G. 1985. Microstructural and microchemical aspects of the solid state decomposition of delta ferrite in austenitic stainless steels. *Metallurgical Transactions A* 16A(8): 1363–1369.

57. Plichta, M., Clark, W., and Aaronson, H.

1984. The nucleation kinetics, crystallography and mechanism of the massive transformation. *Metallurgical Transactions A* 15A(3): 427–435.

58. Hillert, M. 1984. Thermodynamics of the massive transformation. *Metallurgical Transactions A* 15A(3): 411–419.

59. Perepezko, J. 1984. Growth kinetics and mechanism of the massive transformation. *Metallurgical Transactions A* 15A(3): 437–447.

60. Gremaud, M., Katayama, S., Zryd, A., and Matsunawa, A. 1993. Influence of crystallographic and heat flow orientations on growth of cellular dendrites. *ISIJ International* 33(9): 941–948.

## CAN WE TALK?

The *Welding Journal* staff encourages an exchange of ideas with you, our readers. If you'd like to ask a question, share an idea, or voice an opinion, you can call, write, e-mail, or fax. Staff e-mail addresses are listed below, along with a guide to help you interact with the right person.

### Publisher

Jeff Weber  
[jweber@aws.org](mailto:jweber@aws.org), Extension 246  
 General Management,  
 Reprint Permission,  
 Copyright Issues

### Editor

Andrew Cullison  
[cullison@aws.org](mailto:cullison@aws.org), Extension 249  
 Article Submissions

### Senior Editor

Mary Ruth Johnsen  
[mjohnsen@aws.org](mailto:mjohnsen@aws.org), Extension 238  
 Feature Articles

### Associate Editor

Susan Campbell  
[campbell@aws.org](mailto:campbell@aws.org), Extension 244  
 Society News  
 Personnel

### Associate Editor

Ross Hancock  
[rhancock@aws.org](mailto:rhancock@aws.org), Extension 226  
 New Products  
 New Literature

### Production Editor

Zaida Chavez  
[zaida@aws.org](mailto:zaida@aws.org), Extension 265  
 Design and Production

### Advertising Sales Director

Rob Saltzstein  
[salty@aws.org](mailto:salty@aws.org), Extension 243  
 Advertising Sales

### Advertising Production Coordinator

Frank Wilson  
[fwilson@aws.org](mailto:fwilson@aws.org), Extension 465  
 Advertising Production

### Advertising Sales & Promotion Coordinator

Lea Garrigan  
[garrigan@aws.org](mailto:garrigan@aws.org), Extension 220  
 Production and Promotion

### Peer Review Coordinator

Doreen Kubish  
[doreen@aws.org](mailto:doreen@aws.org), Extension 275  
 Peer Review of Research Papers

Welding Journal Dept.  
 550 N.W. LeJeune Rd.  
 Miami, FL 33126  
 (800) 443-9353  
 FAX (305) 443-7404